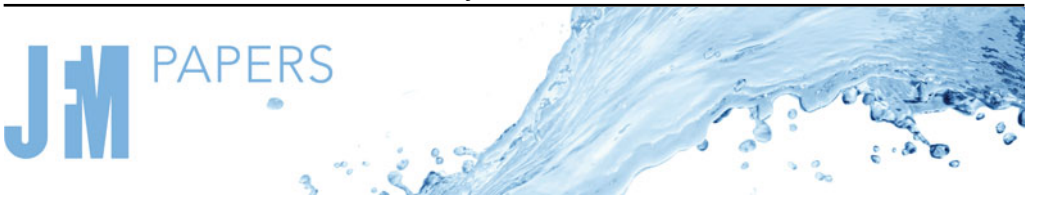
J. Fluid Mech. (2026), *vol.* 1038, A14, doi:10.1017/jfm.2026.11742



Data-driven reduced-order modelling of wake dynamics in hovering flapping flight

Seth Lionetti[1], **Bryan E. Schmidt**[1] **and Chengyu Li**[1]

[1]Department of Mechanical and Aerospace Engineering, Case Western Reserve University, Cleveland, OH 44106, USA

Corresponding author: Chengyu Li, cxl1692@case.edu

(Received 25 August 2025 UTC; revised 7 February 2026 UTC; accepted 18 May 2026 UTC)

As insects flap their wings, they generate complex wake structures critical to their aerodynamic force production. Specific flow structures such as the leading-edge vortex have been studied for decades; however, a complete understanding of the transient dynamics and energy exchange mechanisms in insect wakes remains elusive. To help bridge this gap, we employ data-driven reduced-order modelling techniques to identify a simple and interpretable model for a hovering hawkmoth's wake. We begin by using an in-house immersed-boundary-method computational fluid dynamics solver to simulate hovering hawkmoth flight. We then perform dynamic mode decomposition to distil the resulting flow field into a set of time-varying modes. Finally, we employ sparse regression to identify a model capturing the driving modes' temporal evolution, ranging from quiescent flow to periodic steady state. Notably, the model takes the form of a Stuart–Landau oscillator with higher-order nonlinear terms. The presence of a limit-cycle dynamics suggests a balance between energy input from wing motion and energy lost due to advective energy transfer and viscous dissipation. Using an impulse-based wake survey method, we show that this model provides an accurate estimation (mean absolute error within 3.5 % of body weight) of the hawkmoth's long-term lift production. These findings highlight the significance of stability and energy transfer in flapping-flight aerodynamics, offering a framework for future studies of biological flight systems. Furthermore, by linking the wake dynamics to simple dynamic equations, this work provides inspiration for the design and control of bio-inspired micro-aerial vehicles.

Key words: swimming/flying

© The Author(s), 2026. Published by Cambridge University Press. This is an Open Access article, distributed under the terms of the Creative Commons Attribution licence (https://creativecommons.org/licenses/by/4.0/), which permits unrestricted re-use, distribution and reproduction, provided the original article is properly cited.

https://doi.org/10.1017/jfm.2026.11742 Published online by Cambridge University Press

1. Introduction

Flying insects' wings rapidly shed vortices that interact to form a highly complex, three-dimensional (3-D), and unsteady aerodynamic wake. Understanding the wake dynamics is central to explaining the remarkable efficiency, stability and manoeuvrability inherent to insect flight (Sane 2003; Wang 2005). Much progress has been made in this direction; one prominent discovery is the leading-edge vortex, which is essential for generating the high lift necessary for flight (Ellington *et al.* 1996). Similarly, other studies have highlighted clap-and-fling (Weis-Fogh 1973), wake capture (Dickinson, Lehmann & Sane 1999) and other unsteady mechanisms that contribute to insects' aerodynamic performance (Lehmann 2004). However, beyond simply being a collection of discrete vortices and their interactions, the wake itself is a dynamically evolving system with its own emergent formation, stability and decay properties. Modelling the wake as a whole is a challenging prospect, largely due to the many degrees of freedom necessary for representing its individual components. For example, typical computational fluid dynamics (CFD) simulations involve of the order of 10^6 computational domain cells (Lionetti, Hedrick & Li 2022; Lou *et al.* 2024; Haider *et al.* 2025). Such complexity is a barrier to direct analysis and control strategies and motivates the need for reduced-order modelling (ROM) techniques to isolate the governing dynamics.

Reduced-order modelling provides a powerful suite of tools for simplifying high-dimensional fluid systems. A common first step is modal decomposition, a linear dimensionality reduction technique that expresses the flow as a set of spatial modes with time-varying amplitudes. Various decomposition algorithms have been introduced, each with its own specific aims and properties (e.g. proper orthogonal decomposition (POD), dynamic mode decomposition (DMD) and the discrete Fourier transform) (Taira *et al.* 2017). Following decomposition, the next step is to identify a dynamic model governing the temporal evolution of the modal amplitudes. Traditionally, this is accomplished via Galerkin projection, wherein the Navier–Stokes equations are projected onto the modal basis to yield a system of ordinary differential equations (Holmes 2012). However, Galerkin approaches occasionally suffer from stability and closure issues, motivating a recent shift toward data-driven techniques (Schlegel & Noack 2015; Callaham, Brunton & Loiseau 2022). For example, sparse identification of nonlinear dynamics (SINDy) uses sparse regression to identify a parsimonious and interpretable model for the system dynamics (Brunton *et al.* 2016*a*). Data-driven ROM strategies have been applied to a wide range of fluid dynamics problems, including bluff body wakes (Loiseau, Brunton & Noack 2018), plasma physics (Kaptanoglu *et al.* 2021) and airfoil dynamics (Wang *et al.* 2024). While such methods have proven powerful for canonical flows, their application to complex moving-boundary problems like insect flight has been more limited.

Prior applications of ROM techniques to insect flight have yielded numerous valuable insights, although certain questions pertaining to the wake dynamics remain unanswered. For example, modal decomposition studies have successfully identified dominant flow structures in 3-D flapping-wing wakes, although few have commented on the amplitude dynamics, long-term stability and energy transfer across modes (Liang & Dong 2015; Li, Wang & Dong 2017). Other studies have focused on modelling the insect's wing motion, flight manoeuvres and body oscillations (Liang & Sun 2013; Hedrick, Blandford & Taha 2024); however, such approaches are limited to the insect's kinematics and do not extend to the wake as a whole. Furthermore, quasisteady approaches, while enabling exploration of the dynamic properties of insect flight, do not yield models that can reproduce the wake's transient evolution (Ellington 1984; Brunton, Rowley & Williams 2013). Consequently, ROM of the spatio-temporal dynamics of the full insect wake remains an important, yet underexplored area.

https://doi.org/10.1017/jfm.2026.11742 Published online by Cambridge University Press

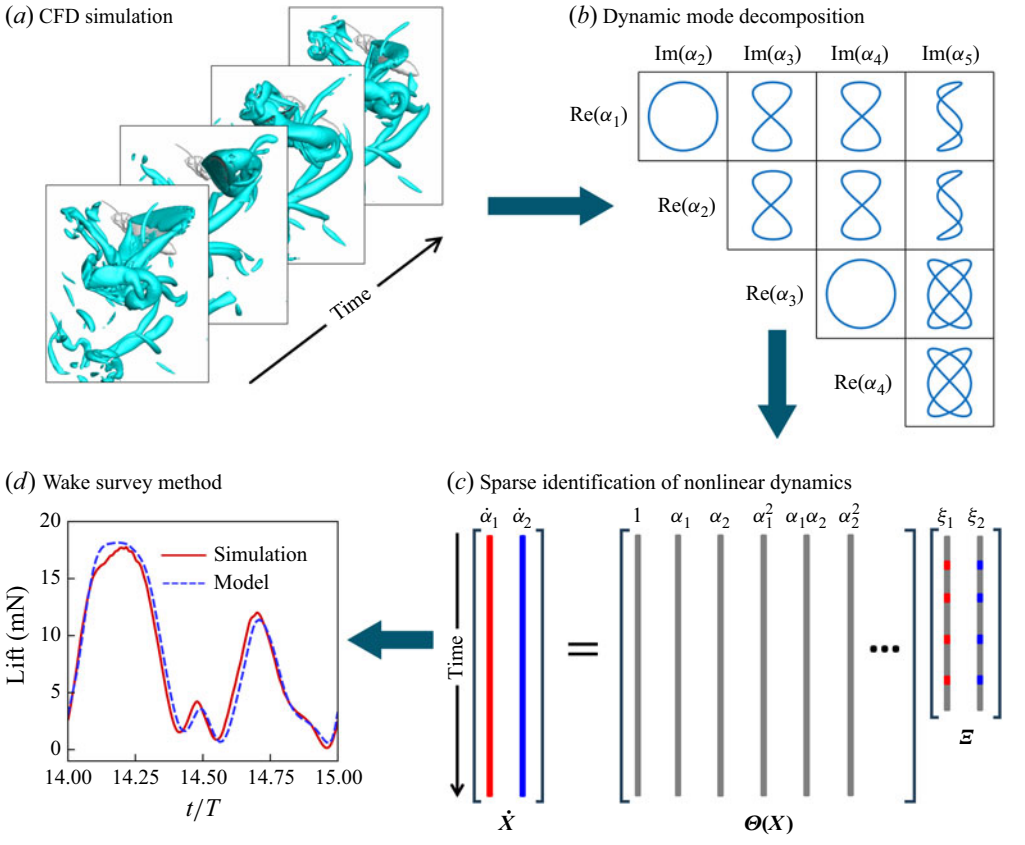


Figure 1. Flowchart of the ROM process. (*a*) The hawkmoth's wake is simulated via CFD. (*b*) The DMD extracts spatio-temporal modes from the flow data. (*c*) A sparse dynamic model is identified for the dominant modes using SINDy. (*d*) The model is validated by comparing its predicted aerodynamic forces, computed using the wake survey method, against the original simulation.

To address these limitations, we employ data-driven ROM techniques to identify an interpretable model for a hovering hawkmoth's wake. We begin by simulating hawkmoth flight using an in-house CFD solver. Then, we employ DMD to reduce the dimensionality of the resulting flow. Given that the DMD amplitudes exhibit strong nonlinear correlations, we use sparse regression to identify modal relationships and further reduce dimensionality, following Loiseau *et al.* (2018) and Callaham *et al.* (2022). Finally, we leverage SINDy to construct a reduced-order dynamic model for the hovering hawkmoth's wake. We validate the model by comparing its prediction of the hawkmoth's aerodynamic forces with the simulated force history. Predicted forces are computed using an impulse-based wake survey method (Noca, Shiels & Jeon 1997). Our overall modelling strategy is described by the flowchart in figure 1. The resulting model aims to provide a simple and physically interpretable representation of the wake's evolution, elucidating the nonlinear mechanisms underlying energy transfer and stability in flapping-flight wakes.

2. Methodology

2.1. *Flow simulation of flapping flight*

To obtain realistic flapping-wing kinematics for our simulation, we use wing motion data from our previous study (Lionetti *et al.* 2022). In that study, we recorded high-speed

https://doi.org/10.1017/jfm.2026.11742 Published online by Cambridge University Press

videos of a *Manduca sexta* hawkmoth hovering while feeding from an artificial flower, then transferred the recordings into Autodesk Maya to create a detailed 3-D reconstruction of the hawkmoth's wing motion. This reconstructed model captures the natural bending and twisting deformations of the wings during flight. Full details of the experimental set-up, kinematic reconstruction procedure and wing Euler angle data can be found in Lionetti *et al.* (2022).

We simulate hovering flight using an in-house immersed-boundary-method CFD solver. The solver numerically evaluates the unsteady 3-D viscous incompressible Navier–Stokes equations given by

$$\nabla \cdot \boldsymbol{u} = 0,$$
$$\frac{\partial \boldsymbol{u}}{\partial t} + (\boldsymbol{u} \cdot \nabla)\,\boldsymbol{u} = -\frac{1}{\rho}\nabla p + \nu \nabla^2 \boldsymbol{u}, \tag{2.1}$$

where $\boldsymbol{u}$ is the velocity, p is the pressure, ρ is the density and ν is the kinematic viscosity. These equations are discretised in space using a second-order central differencing scheme, where the primitive variables $\boldsymbol{u}$ and p are collocated at the cell centres. A fractional-step pressure-correction method is employed to advance the equations in time. Boundary conditions at the immersed bodies are enforced via a ghost-cell procedure (Mittal *et al.* 2008), and movement of the immersed bodies (i.e. the flapping wings) is prescribed according to the aforementioned kinematic reconstruction. The Reynolds number used in the simulation is 7337, defined as $Re = \overline{U_{tip}} c/\nu$, where $\overline{U_{tip}} = 4.9764\,\mathrm{ms}^{-1}$ is the average wing-tip velocity, $c = 2.30\,\mathrm{cm}$ is the average wing chord length and $\nu = 1.56 \times 10^{-5}\ \mathrm{m}^2\ \mathrm{s}^{-1}$ is the kinematic viscosity of air.

Additional details regarding simulation set-up and grid independence are located in Appendix A, and our previous paper includes a validation based on force history (Lionetti *et al.* 2022). We run the simulation for a total of fifteen flapping cycles using identical wing kinematics for each cycle, thereby capturing the full evolution of the wake from quiescence at $t/T = 0$ to periodic steady state, where T represents the period of one flapping cycle. This extended simulation duration is critical for developing a robust SINDy-based reduced-order model, as it provides a sufficiently rich dataset to capture both the transient and post-transient wake dynamics. In Appendix B, we demonstrate that the forces generated by the flapping wing become periodic after approximately five flapping cycles, while it takes nine cycles for the wake itself to achieve periodicity.

2.2. *Dynamic mode decomposition*

A wide variety of decomposition methods have been proposed for dimensionality reduction in fluid dynamics (Lumley 1967; Schmid 2010; Sieber, Paschereit & Oberleithner 2016). In this work, we elect to use DMD for its ability to identify spatio-temporally coherent modes that oscillate with a fixed frequency. This attribute makes it ideal for studying flapping-wing wakes which are dominated by a single frequency (i.e. the hawkmoth's flapping frequency, $f = 25.6\,\mathrm{Hz}$). Specifically, we employ the popular Exact DMD algorithm introduced by Tu (2013). Due to the widespread adoption of this method, we refrain from reproducing detailed derivations here, instead providing a brief overview of its theoretical foundations.

Dynamic mode decomposition approximates the eigendecomposition of the linear operator $\boldsymbol{A}$ that advances a system (in this case $\boldsymbol{U}$, the fluid velocity components stored at all computational domain cells) forward in time

$$\boldsymbol{U}_{t+\Delta t} = \boldsymbol{A}\boldsymbol{U}_t. \tag{2.2}$$

https://doi.org/10.1017/jfm.2026.11742 Published online by Cambridge University Press

However, for fluid dynamic systems, the dimensionality of $\boldsymbol{A}$ is often prohibitively large, making direct computation infeasible. Exact DMD therefore leverages the singular value decomposition to derive the reduced-order operator $\tilde{\boldsymbol{A}}$. Spatial DMD modes are obtained from eigenvectors of $\tilde{\boldsymbol{A}}$, and their temporal dynamics is determined by the corresponding eigenvalues. Each DMD mode is associated with a fixed frequency, growth/decay rate and initial amplitude. Based on this information, the time dynamics may be compiled into a coefficient matrix $\boldsymbol{\alpha}_{N\times M}$, where N is the total number of modes and M is the number of time steps. Similarly, the spatial modes are arranged as columns of $\boldsymbol{\Phi}_{D\times N}$, where D is the size of the spatial domain. Then, $\boldsymbol{U}=\boldsymbol{\Phi}\boldsymbol{\alpha}$, or equivalently,

$$\boldsymbol{U}\,(\boldsymbol{x},t)=\sum_{i=0}^{N-1}\boldsymbol{\Phi}_i\,(\boldsymbol{x})\,\alpha_i\,(t)\,. \tag{2.3}$$

Some information pertaining to the system dynamics is provided by the results of DMD. For example, oscillatory flow components are captured by complex conjugate mode pairs, while real-valued modes are inherently non-oscillatory. In addition, the growth or decay of each mode $\boldsymbol{\Phi}_i$ is determined by the complex magnitude of its corresponding eigenvalue λ_i. Eigenvalues with magnitude greater than one indicate unstable growth, while eigenvalues with magnitude less than one indicate decay. Eigenvalues that lie on or very close to the complex unit circle denote constant-amplitude stable modes. Furthermore, provided all spatial modes generated by DMD are l^2-normalised, the average energy of each mode is approximated by

$$E_i=\overline{|\alpha_i|^2}, \tag{2.4}$$

where overbar denotes the time average. Note we use E_i only as a relative mode-importance metric; it is not an exact partition of total kinetic energy as in POD (Taira *et al.* 2017).

2.3. *Sparse regression*

The modal basis resulting from DMD provides a compact coordinate system for modelling the system dynamics. The goal of a reduced-order model is then to identify a parsimonious system of dynamic equations governing $\boldsymbol{\alpha}(t)$. A well-established framework for this process is SINDy (Brunton *et al.* 2016*a*). The problem posed by SINDy is formulated as

$$\dot{\boldsymbol{X}}=\boldsymbol{\Theta}\,(\boldsymbol{X})\,\boldsymbol{\Xi}, \tag{2.5}$$

where $\boldsymbol{X}$ contains the time history of the input variables (here, the DMD coefficients $\boldsymbol{\alpha}$); $\dot{\boldsymbol{X}}$ is its time derivative; $\boldsymbol{\Theta}$ is a library of candidate model terms, expressed as nonlinear functions of the input variables; and $\boldsymbol{\Xi}$ is a sparse coefficient matrix denoting which columns of $\boldsymbol{\Theta}$ are active. Sparsity promotion is employed to drive as many entries in $\boldsymbol{\Xi}$ to zero as possible, resulting in the simplest model that accurately describes the system.

Many sparsity-promoting regression techniques exist for evaluating (2.5) (de Silva *et al.* 2020). In this work, we employ forward regression orthogonal least squares (FROLS), which belongs to the family of NARMAX methods (i.e. nonlinear autoregressive moving average models with exogenous inputs). We closely follow the implementation found in Billings (2013), albeit with minor modifications to extend the algorithm to the complex domain. Specifically, because DMD yields complex-valued data and coefficients, standard FROLS implementations cannot be directly applied. We therefore introduce adjustments such as employing the Hermitian inner product ($\langle \boldsymbol{a},\boldsymbol{b}\rangle=\boldsymbol{b}^H\boldsymbol{a}$) for projection operations, using the squared magnitude $|g|^2$ to compute the error reduction ratio, and applying

https://doi.org/10.1017/jfm.2026.11742 Published online by Cambridge University Press

complex arithmetic throughout the algorithm. These modifications ensure accurate sparse identification for systems with a complex-valued dynamics.

The FROLS method is a greedy algorithm that iteratively selects model terms (columns of $\boldsymbol{\Theta}$) that best explain the variance in the target variables $\dot{\boldsymbol{X}}$. During each iteration, candidate terms are orthogonalised with all previously selected terms using the Gram–Schmidt process, ensuring linear independence. The library $\boldsymbol{\Theta}$ may be populated with any type of functions of the input variables $\boldsymbol{X}$; in this work, we employ polynomial functions up to order ten. The algorithm stops either when all candidate terms have been selected, or when the unexplained variance in the target variables falls below a user-specified tolerance (we use 10^{-6}).

2.4. *Wake survey method*

Once a suitable model has been identified, the full-order system is reconstructed by integrating the model forward in time to find $\boldsymbol{X}_{pred}$, whose columns are predicted coefficients $\boldsymbol{\alpha}_{pred}$. These coefficients are then substituted into (2.3) to regain the full velocity field $\boldsymbol{U}_{pred}$. There are several ways of comparing $\boldsymbol{U}_{pred}$ with the actual velocity $\boldsymbol{U}$ obtained from our simulation. Perhaps the most common is computing the l^2-norm-based prediction error $||\boldsymbol{U} - \boldsymbol{U}_{pred}||_2$; however, the physical significance of this metric is not readily interpretable in the context of flapping-wing wakes and is cumbersome because of the large number of points in the spatial domain. An average value of this quantity over the domain or the root-mean-square error is likewise avoided because it can be strongly influenced by a few high-error outliers. We instead use the predicted flow field $\boldsymbol{U}_{pred}$ to compute the aerodynamic lift and drag produced by the hawkmoth, which may then be directly compared against the true force history from the CFD simulation.

Accurately calculating aerodynamic forces on an immersed body typically requires pressure information. However, because our SINDy-based model predicts only the velocity field, we employ a wake survey method that relies solely on velocity data and their derivatives without the need for pressure. This approach, introduced by Noca *et al.* (1997), is derived from the impulse equation. Forces on a body are given by

$$\boldsymbol{F} = -\frac{1}{d-1}\frac{\mathrm{d}}{\mathrm{d}t}\int_{V(t)} \boldsymbol{x}\times\boldsymbol{\omega}\mathrm{d}V + \oint_{S(t)} \boldsymbol{n}\cdot\boldsymbol{\gamma}_{imp}\mathrm{d}S - \frac{1}{d-1}\frac{\mathrm{d}}{\mathrm{d}t}\oint_{S_b(t)} \boldsymbol{x}\times(\boldsymbol{n}\times\boldsymbol{u})\,\mathrm{d}S, \tag{2.6}$$

where $V(t)$ is a non-material bounding volume containing the body; $S(t)$ is the corresponding bounding surface; $S_b(t)$ is the body surface; d is the number of spatial dimensions (in this case, 3); and $\boldsymbol{n}$, $\boldsymbol{x}$, $\boldsymbol{u}$ and $\boldsymbol{\omega}$ are normal, position, velocity and vorticity vectors, respectively. The term $\boldsymbol{\gamma}_{imp}$ is defined as

$$\begin{aligned}\boldsymbol{\gamma}_{imp} = {} & \frac{1}{2}u^2\boldsymbol{I} - \boldsymbol{u}\boldsymbol{u} - \frac{1}{d-1}(\boldsymbol{u}-\boldsymbol{u}_s)(\boldsymbol{x}\times\boldsymbol{\omega}) + \frac{1}{d-1}\boldsymbol{\omega}(\boldsymbol{x}\times\boldsymbol{u}) \\ & + \frac{1}{d-1}[\boldsymbol{x}\cdot(\nabla\cdot\boldsymbol{T})\boldsymbol{I} - \boldsymbol{x}(\nabla\cdot\boldsymbol{T})] + \boldsymbol{T},\end{aligned} \tag{2.7}$$

where $\boldsymbol{u}_s$ is the velocity of the bounding surface, $\boldsymbol{I}$ is the identity tensor, and $\boldsymbol{T}$ is the viscous stress tensor.

Our implementation of Noca's method has been validated in several previous studies (Liang & Dong 2015; Li *et al.* 2017). Furthermore, to ensure its suitability for this problem, we first verify in Appendix C that this technique can accurately predict aerodynamic forces when applied to our full CFD simulation data. Having established this validation, we can

https://doi.org/10.1017/jfm.2026.11742 Published online by Cambridge University Press

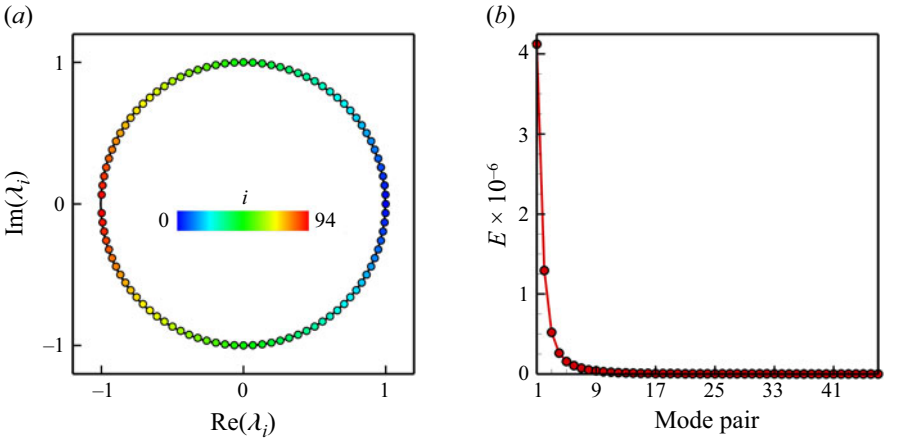


Figure 2. The DMD eigenvalue and energy spectra. (*a*) Eigenvalues of all 95 identified modes are plotted on the complex plane, with the unit circle shown in black. (*b*) Energy content, calculated using (2.4), is shown for the 47 oscillatory mode pairs.

then apply the same wake survey method to the velocity field predicted by the SINDy model, using the calculated forces as an assessment of the model's performance. Finally, we note that the wake survey method is not the only procedure for velocity-based force reconstruction. For example, the force partitioning method, another widely adopted technique, enables decomposition of forces into constituent components induced by vorticity, added-mass effects, body movement and viscosity (Menon & Mittal 2021*a*, *b*). For this study, however, we elect to employ Noca's wake survey method for its simplicity, demonstrated accuracy (Appendix C) and suitability for our needs (i.e. evaluation of ROM error).

3. Results and discussion

3.1. *Dimensionality reduction*

We begin by performing DMD on $\boldsymbol{U}$, the fluid velocity results from our CFD simulation (described in § 2.1). However, decomposing the entire simulated flow history ($t/T = 0.0$–15.0) is computationally expensive, and the resulting large number of modes would not constitute a suitably low-order basis for sparse regression. We therefore decompose only the fifteenth and final simulated flapping cycle ($t/T = 14.0$–15.0), proceeding under the assumption that modes from the periodic portion of the flow history can also serve as a reasonable basis for modelling the transient dynamics. This assumption is motivated by previous studies that identify a low-order attractor-based dynamics in flows involving periodic vortex shedding (Wiliamson 1996; Noack *et al.* 2003); its validity will be evaluated in subsequent sections. See Appendix B for demonstration that the wake achieves periodicity before the fifteenth flapping cycle.

As inputs for the DMD algorithm, we select 97 equally spaced snapshots ranging between $t/T = 14.0$ and 15.0, inclusive. Decomposition yields a total of $N = 95$ modes, including a real-valued mode ($\boldsymbol{\Phi}_0$) capturing the mean flow, as well as 47 complex conjugate mode pairs ($\boldsymbol{\Phi}_{1,2}, \boldsymbol{\Phi}_{3,4}, \ldots, \boldsymbol{\Phi}_{93,94}$) representing oscillations at different frequencies. A single mode with eigenvalue $\lambda_i = -1$ and negligible energy content represents a sampling frequency alias and is therefore omitted from consideration. The eigenvalues λ_i corresponding to each mode are displayed in figure 2(*a*). As expected, all eigenvalues lie on or very close to the complex unit circle, indicating that modal amplitudes neither grow nor decay in time. This is consistent with the assumption that

https://doi.org/10.1017/jfm.2026.11742 Published online by Cambridge University Press

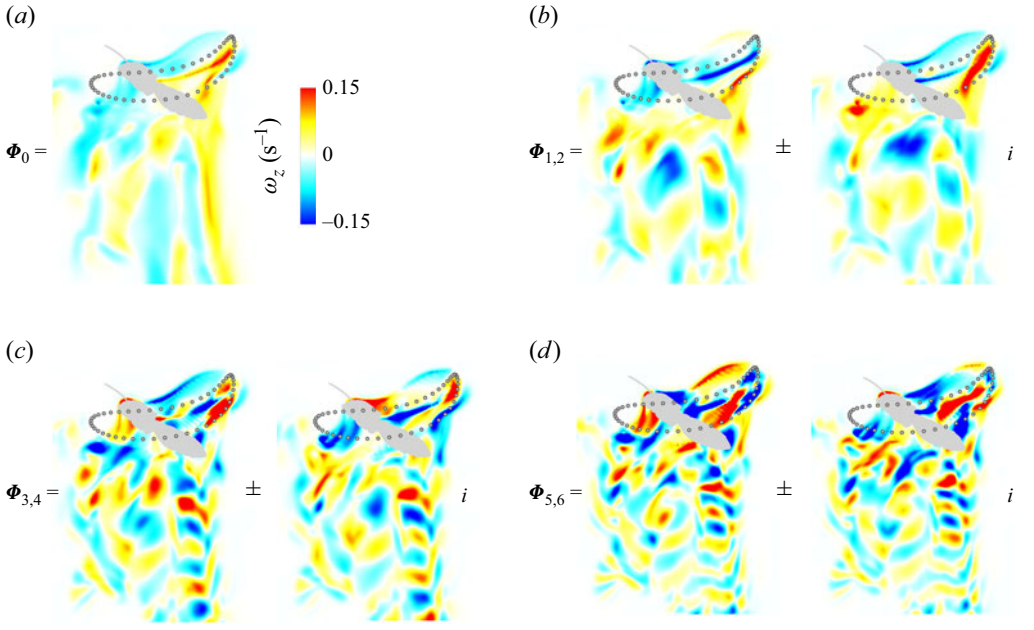


Figure 3. Spatial structures of the first seven DMD modes, visualised by mid-wingspan vorticity ω_z. Results are included for (*a*) the mean mode $\boldsymbol{\Phi}_0$ and (*b–d*) the first three oscillatory mode pairs, $\boldsymbol{\Phi}_{1,2}$ to $\boldsymbol{\Phi}_{5,6}$. An outline of the hawkmoth's body, as well as 48 equitemporally spaced points from its wing-tip trajectory, are overlaid as a reference.

the wake dynamics during the selected flapping cycle is periodic. Figure 2(*b*) presents the energy spectrum of the oscillatory modes, plotting the combined energy for each complex conjugate pair. Modes are ordered by decreasing energy E_i, which is shown to be highly concentrated within the first few pairs. Figure 3 depicts the mid-wingspan vorticity fields corresponding to the mean mode $\boldsymbol{\Phi}_0$ and the first three oscillatory pairs ($\boldsymbol{\Phi}_{1,2}$, $\boldsymbol{\Phi}_{3,4}$ and $\boldsymbol{\Phi}_{5,6}$). The spatial structures reveal characteristic vortex shedding patterns, with the pairs $\boldsymbol{\Phi}_{3,4}$ and $\boldsymbol{\Phi}_{5,6}$ capturing finer-scale features. Additional insight into the wake dynamics is gained by examining the temporal coefficients. Figure 4 shows the parametric relationships between the coefficients corresponding to the first eight modes, α_1 to α_8. We observe that modal relationships take the form of Lissajous curves, indicating that all modes represent harmonics of a single fundamental frequency. Specifically, the first mode pair $\alpha_{1,2}$ fluctuates at the hawkmoth's flapping frequency $f = 25.6\,\text{Hz}$, the second pair $\alpha_{3,4}$ fluctuates at $2f$, the third pair $\alpha_{5,6}$ at $3f$ and so on.

This Fourier-like harmonic structure supports our initial assumption that the dynamics is periodic after fifteen flapping cycles. More significantly, it suggests that the latent dimensionality of the system is much lower than the $N = 95$ modal bases resulting from DMD. Exact DMD and related algorithms generate only linear decompositions, wherein the full system state is expressed as a superposition of time-varying modes (2.3). As a result, nonlinear modal relationships such as those visible in figure 4 cannot be identified by such techniques. However, there exist numerous nonlinear dimensionality reduction (or manifold learning) methods that may be employed for this purpose (Tenenbaum, Silva & Langford 2000; Champion *et al.* 2019; Fresca & Manzoni 2022). In this work, we follow the simple approach introduced by Loiseau *et al.* (2018) and Callaham *et al.* (2022). Because all modes are harmonics of a single frequency f, we employ sparse regression to express higher-frequency modes as polynomial functions of the first mode pair $\alpha_{1,2}$.

https://doi.org/10.1017/jfm.2026.11742 Published online by Cambridge University Press

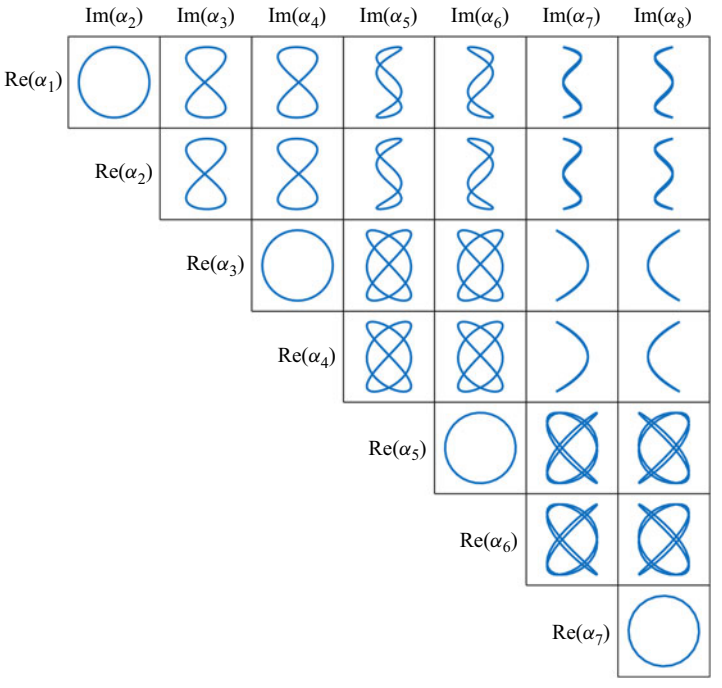


Figure 4. Parametric plots of the DMD temporal coefficients α_i for the first four oscillatory mode pairs.

Treating coefficients $\alpha_{1,2}$ as inputs and all other coefficients as target variables, we use FROLS to identify the following nonlinear relationships

$$\begin{aligned} \alpha_0 &= \beta_0 \alpha_1 \alpha_2, \\ \alpha_3 = \beta_3 \alpha_1^2, \quad \alpha_4 &= \beta_4 \alpha_2^2, \\ \alpha_5 = \beta_5 \alpha_1^3, \quad \alpha_6 &= \beta_6 \alpha_2^3, \\ &\vdots \\ \alpha_{93} = \beta_{93} \alpha_1^{47}, \quad \alpha_{94} &= \beta_{94} \alpha_2^{47}, \end{aligned} \tag{3.1}$$

where β_i are complex constants (tabulated in Appendix D).

These relationships provide evidence of an energy cascade from the fundamental frequency f, driven by the hawkmoth's wing motion, to higher harmonics. Specifically, they capture the effects of triadic modal interactions arising from the quadratic nonlinearity in the convection term, $(\boldsymbol{u} \cdot \nabla)\boldsymbol{u}$, of the Navier–Stokes equations (2.1) (Schmidt 2020; Callaham *et al.* 2022; Kinjangi & Foti 2023). Self-interaction of the fundamental mode pair $\alpha_{1,2}$ drives the second harmonic $\alpha_{3,4}$, such that $\alpha_3 \propto \alpha_1^2$ and $\alpha_4 \propto \alpha_2^2$. In turn, the second harmonic mixes with the fundamental to drive the third (e.g. $\alpha_5 \propto \alpha_3 \alpha_1$), and so on. Algebraically eliminating all modal coefficients save for the fundamental pair yields the high-order monomials (3.1) identified by FROLS. This result is consistent with the modal energy spectrum shown in figure 2(*b*). Kinetic energy is injected into the flow at the fundamental frequency f and is sequentially distributed to higher harmonics; consequently, the flow's energy is concentrated within the lower-frequency modes. Visual comparison of the spatial modes in figure 3 further supports this interpretation: the dominant mode pair ($\boldsymbol{\Phi}_{1,2}$) captures large-scale vortical motion, while higher-frequency modes ($\boldsymbol{\Phi}_{3,4}$, etc.) capture finer spatial structures, consistent with an

https://doi.org/10.1017/jfm.2026.11742 Published online by Cambridge University Press

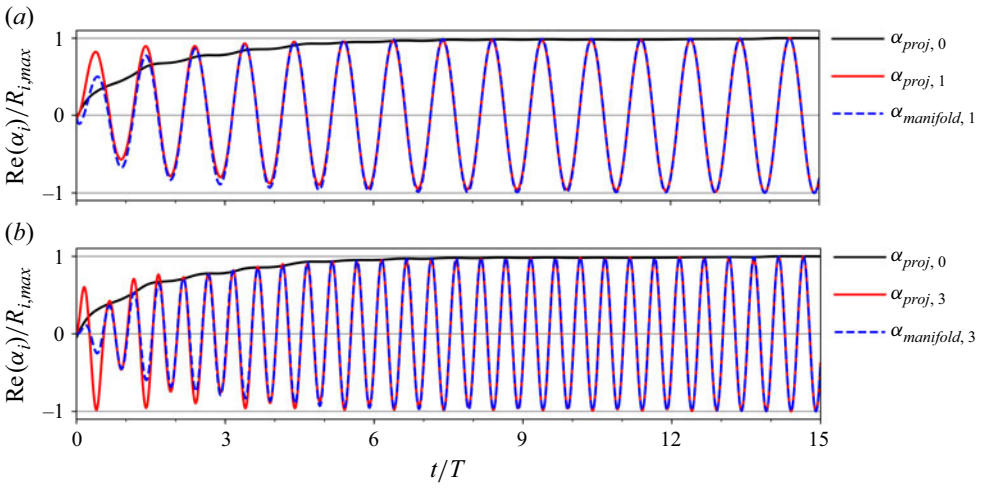


Figure 5. Temporal evolution of the DMD coefficients throughout the wake's transient evolution. Plots compare the original projected coefficients ($\boldsymbol{\alpha}_{proj}$, red) with the manifold-constrained coefficients ($\boldsymbol{\alpha}_{manifold}$, blue) used for model identification. Only the real components of the coefficients are shown, and coefficient amplitudes R_i are normalised by their respective maxima. Results are included for (*a*) the fundamental mode α_1 and (*b*) its first harmonic α_3. Also included in both panels is the contribution from the mean mode ($\alpha_{proj,0}$, black).

energy cascade from large to small scales. Because (3.1) allows all modal coefficients to be reconstructed from $\alpha_{1,2}$, the effective system dimension collapses to just these two active degrees of freedom. The goal of our reduced-order model is therefore to track the transient evolution of this driving mode pair from quiescent flow (where $\alpha_{1,2} = 0$) to periodic steady state (i.e. figure 4).

3.2. *Model identification*

As stated in § 3.1, we perform DMD only on the final flapping cycle ($t/T = 14.0$–15.0), during which the dynamics is periodic. To obtain the transient evolution of the active degrees of freedom $\alpha_{1,2}$, it is necessary to project the full simulation history ($t/T = 0.0$–15.0) onto the modal basis $\boldsymbol{\Phi}$. Unlike other decomposition techniques, such as POD, DMD does not guarantee orthogonal modes (Taira *et al.* 2017). Projection onto $\boldsymbol{\Phi}$ therefore requires taking its pseudoinverse $\boldsymbol{\Phi}^+$

$$\boldsymbol{\alpha}_{proj} = \boldsymbol{\Phi}^+ \boldsymbol{U}. \tag{3.2}$$

Here, $\boldsymbol{\alpha}_{proj}$ are the temporal coefficients resulting from projection, and $\boldsymbol{U}$ contains 1440 fluid velocity snapshots ranging between $t/T = 1/96$ and 15.0, inclusive.

Figure 5 shows these projected coefficients, normalised by their respective maximum amplitudes. Specifically, it illustrates the temporal evolution of the mean mode α_0 (black line), alongside the real components of the driving mode pair $\mathrm{Re}(\alpha_{1,2})$ and its first harmonic $Re(\alpha_{3,4})$ (red lines). The amplitude of the mean mode rapidly and monotonically increases, reaching a maximum after approximately six flapping cycles; this trajectory is evidence of the wake's approach towards a periodic steady-state dynamics. The amplitudes of $\alpha_{1,2}$ and $\alpha_{3,4}$ likewise saturate after several flapping cycles, although their initial growth is non-monotonic and exhibits large fluctuations.

To enable an interpretable and computationally efficient model, we prioritise capturing the emergence and saturation of the dominant wake structures associated with the fundamental frequency f, rather than attempting to model the full transient dynamics

https://doi.org/10.1017/jfm.2026.11742 Published online by Cambridge University Press

across all 95 projected coefficients $\boldsymbol{\alpha}_{proj}$. Directly modelling this high-dimensional transient dynamics is intractable due to early deviations from the low-dimensional harmonic structure identified in (3.1). To address this, and motivated by classical weakly nonlinear analyses and vortex shedding models (Herbert 1988; Noack *et al.* 2003), we enforce the relationship $\alpha_0 \propto \alpha_1\alpha_2$ (identified in (3.1)) throughout the transient. This assumption is grounded in the physical principle that mean flow distortions typically scale quadratically with oscillatory mode amplitudes due to the quadratic nonlinearity of the Navier–Stokes equations. Leveraging the smooth growth of the mean mode $\alpha_{proj,0}$, we scale the amplitudes of the fundamental pair: $|\alpha_{1,2}| = \sqrt{\alpha_0/\beta_0}$. Then, the adjusted $\alpha_{1,2}$ coefficients dictate the evolution of all higher harmonics through their established dependencies in (3.1). This choice effectively constrains the dynamics to a physically interpretable 2-D manifold, preserving key nonlinear interactions while greatly reducing model complexity. As shown by the manifold-constrained trajectories (blue lines in figure 5), this approach smooths amplitudinal growth in the driving mode pair $\alpha_{1,2}$ and its first harmonic $\alpha_{3,4}$. Significant deviations from the original projected coefficients occur primarily during the early transient phase ($t/T \approx 0.0$–1.5). The implications and theoretical underpinnings of this modelling choice will be further addressed in § 3.4.

Having established the complete transient histories of the active degrees of freedom $\alpha_{1,2}$ (blue line in figure 5(*a*)), it remains to identify a sparse dynamic model governing their evolution. For this task, we rely on SINDy, as formulated by (2.5). We differentiate $\alpha_{1,2}$ to obtain columns of $\dot{\boldsymbol{X}}$, and we populate the library of candidate terms $\boldsymbol{\Theta}$ with all polynomial functions of $\alpha_{1,2}$ up to order ten. Figure 6 shows the results of successive FROLS iterations, each incorporating an additional model term. Initially, adding terms improves the prediction of the coefficients $\alpha_{1,2}$. However, increasing the number of terms beyond four does not yield noticeable benefits. Furthermore, after four iterations, the stopping criterion for the algorithm falls below our specified tolerance of 10^{-6}. The resulting sparse four-term dynamic model takes the form

$$\begin{aligned} \dot{\alpha_1} &= \sum_{n=0}^{3} \mu_n \alpha_1 \, |\alpha_1|^{2n} \,, \\ \dot{\alpha_2} &= \dot{\alpha_1}^{*}, \end{aligned} \tag{3.3}$$

where μ_n are complex constants (listed in table 1), and $*$ denotes the complex conjugate. We note that, of the 66 terms initially in the library $\boldsymbol{\Theta}$, only four are retained in the final model. This degree of sparsity promotion ensures that (3.3) is the simplest model capable of accurately representing the dynamics.

To examine this model in detail, figure 7 shows the full trajectory of the driving coefficients $\alpha_{1,2}$, obtained by integrating the model forward in time following a small initial perturbation. The system's initial quiescent state and long-term periodic response are marked in blue and red, respectively; between these extremes, the coefficients spiral outward rapidly. The full-order system is reconstructed by first applying the nonlinear coefficient relationships identified in (3.1), then via the linear superposition of spatial modes given by (2.3). As described in § 2.4, we validate the model by using the wake survey method to compute the aerodynamic forces generated by the hawkmoth. In figure 8, the predicted forces are compared against the real forces obtained from our CFD simulation. We observe that, during the early transient period ($t/T \approx 0.0$–1.5), the model only captures the general trend of the hawkmoth's lift and drag, while generally underestimating their magnitude. However, model accuracy improves greatly as time progresses, yielding a nearly perfect lift prediction (mean absolute error of 0.66 mN, within 3.5 % of body

https://doi.org/10.1017/jfm.2026.11742 Published online by Cambridge University Press

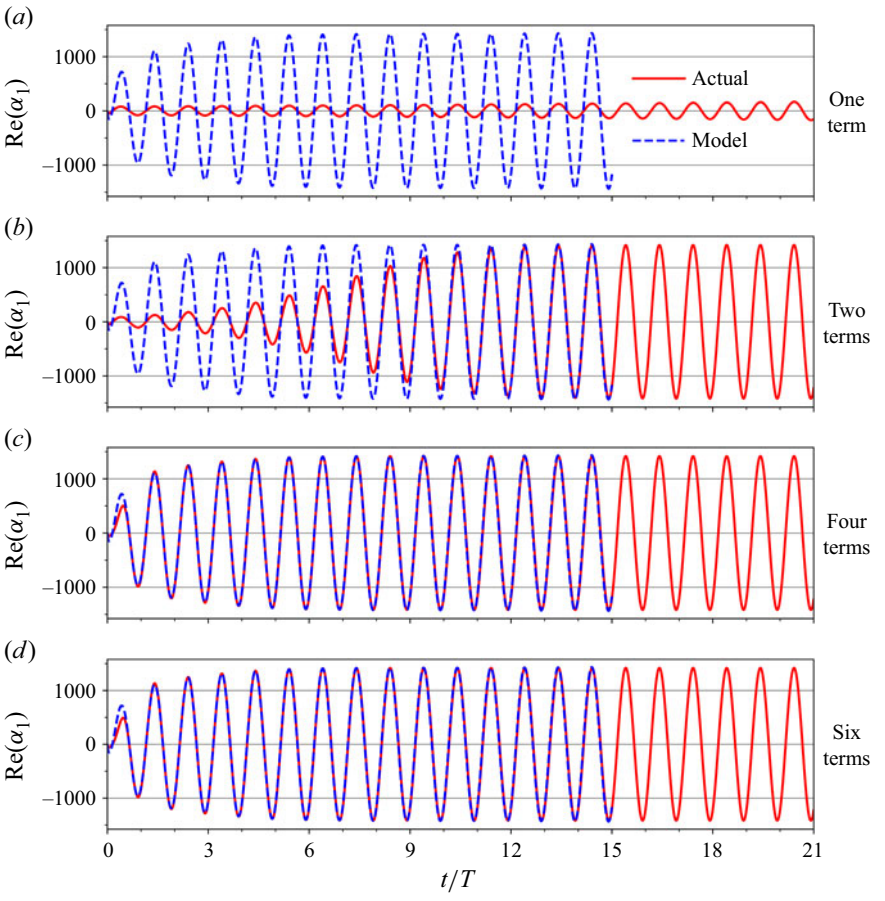


Figure 6. Model improvement with successive SINDy terms. Plots compare the actual temporal evolution of the driving mode coefficient Re(α_1) (blue) with the model's prediction (red) using (*a*) one, (*b*) two, (*c*) four and (*d*) six terms. To assess the model's predictive capability, it is integrated for an additional six cycles beyond our simulation timespan ($t/T = 0.0$–15.0).

weight) after four flapping cycles. For reference, the end of the fourth flapping cycle ($t/T = 4.0$) is marked with a green 'x' in figure 7. See Appendix E for further discussion of modelling error. To evaluate the model's long-term response, we integrate it far beyond the timespan of our simulation ($t/T = 0.0$–15.0). After 200 flapping cycles, the predicted forces still align well with the earlier simulated forces, as expected given the wake's periodicity. Finally, figure 9 compares the simulated Q-criterion wake structures with those predicted by the model. The Q-criterion is defined as the second invariant of the velocity gradient tensor ∇U. During the fourth flapping cycle (figure 9*a*), we observe that the model does not capture the full leading-edge vortex attached to the hawkmoth's wing, contributing to the observed force underprediction in figure 8(*a*). However, model accuracy improves by the ninth cycle (figure 9*b*), and during the fifteenth cycle (figure 9*c*), the model-derived structures exhibit few visible differences compared with those from the simulation.

3.3. *Physical interpretation*

The identified model (3.3) corresponds to the normal form of a supercritical Hopf bifurcation, truncated after the seventh-order nonlinear term; isolating the first two terms

https://doi.org/10.1017/jfm.2026.11742 Published online by Cambridge University Press

μ_0	$4.9419 + 6.2754i$
μ_1	$(-8333.3 + 5.5559i) \times 10^{-9}$
μ_2	$(4774.0 - 3.1056i) \times 10^{-15}$
μ_3	$(-9210.4 - 5.7768i) \times 10^{-22}$

Table 1. Coefficients μ_n corresponding to the reduced-order model (3.3) identified by SINDy.

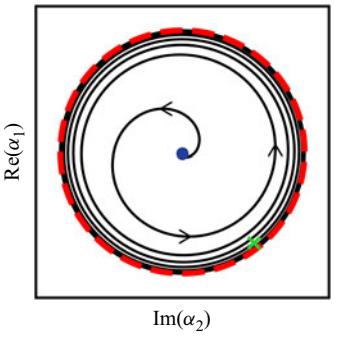


Figure 7. Phase portrait of the driving coefficients $\alpha_{1,2}$, obtained by integrating the model (3.3) forward in time. The system's initial quiescent state and eventual periodic response are shown in blue and red, respectively. For reference, the position corresponding to the end of the fourth flapping cycle ($t/T = 4.0$) is marked with a green 'x'. Arrows indicate the direction of the coefficients' trajectory.

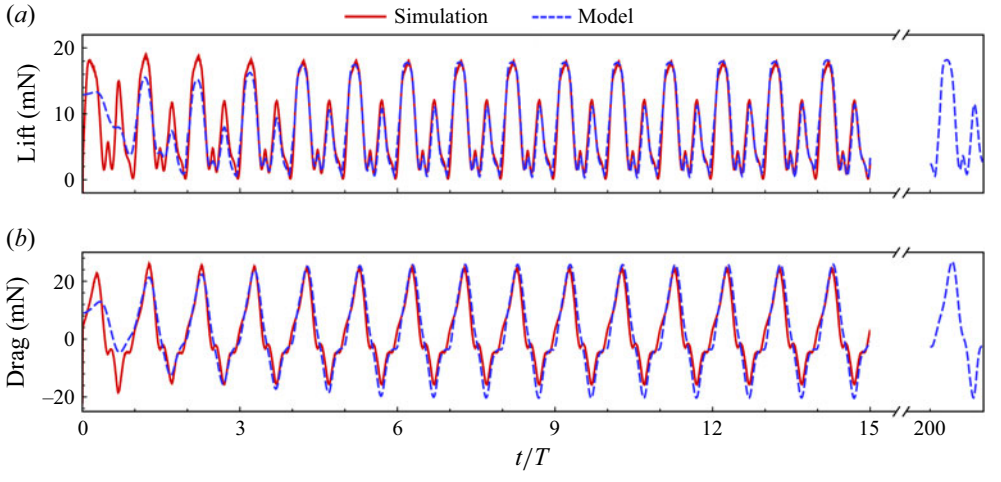


Figure 8. Model validation via aerodynamic force prediction. Shown are the (*a*) lift and (*b*) drag forces computed from the full CFD simulation (red) and the forces predicted by the model with 4 terms (blue).

($n = 0, 1$) yields the standard Stuart–Landau oscillator. As expected for such systems, the phase portrait of the driving coefficients $\alpha_{1,2}$ (figure 7) is strongly indicative of a limit-cycle dynamics. We investigate the limit cycles predicted by the model by finding the equilibrium amplitudes, $R = |\alpha_1|$. These correspond to the non-negative real roots R_0 of the amplitude equation $\dot{R} = H(R) = 0$, with $H(R)$ defined as

$$H(R) = \sum_{n=0}^{3} \mathrm{Re}(\mu_n) R^{2n+1}. \tag{3.4}$$

https://doi.org/10.1017/jfm.2026.11742 Published online by Cambridge University Press

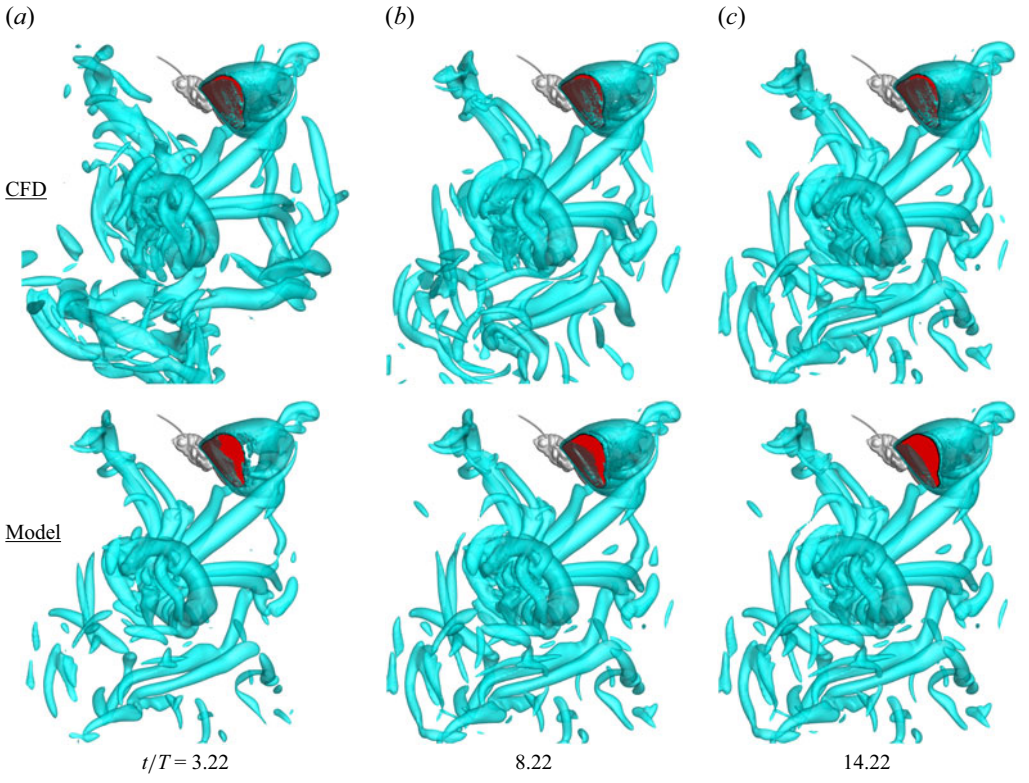


Figure 9. Visual comparison of wake structures. Q-criterion isosurfaces are displayed for the full CFD simulation (top) and the wake predicted by the model (bottom). Wake structures are shown at (*a*) $t/T = 3.22$, (*b*) 8.22 and (*c*) 14.22, corresponding to the time instant of maximum lift production within each cycle. The hawkmoth's body is shown in grey, while the simulated flapping wing is highlighted in red.

Then, stability is determined by the sign of $H'(R_0)$: negative values indicate stable solutions, and *vice versa*. Using this technique, we identify an unstable fixed point at the origin ($\alpha_{1,2} = 0$) and a single stable limit cycle with amplitude $R_{max} = 1417.76$. We also compute a settling time of $t_s/T = 4.42$, defined as the time required for $|\alpha_{1,2}|$ to reach and remain within ± 5 % of R_{max}. This value indicates that it takes approximately 4.42 flapping cycles (0.173 s) for the wake to stabilise. Note that settling time is sensitive to the threshold chosen for limit-cycle convergence; if ± 1 % is used instead, t_s/T increases to 8.16, which aligns with the time required for the wake to achieve periodicity (Appendix B).

These findings are in alignment with the trajectory of the coefficients $\alpha_{1,2}$ (figure 7), as well as the long-term stability and periodicity of the hawkmoth's force generation (figure 8). Furthermore, we observe that the model's force prediction improves as the system approaches the identified limit cycle. This increase in accuracy is consistent with concepts from the study of dissipative partial differential equations, such as the slaving principle and the conjectured existence of inertial manifolds (Haken 1977; Sirovich, Knight & Rodriguez 1990; Temam 2012). These theories posit that, once sufficient spectral separation is achieved, the fast variables (in this case, the higher harmonic DMD modes) become functions of a few slow driving variables (coefficients $\alpha_{1,2}$). Consequently, the long–term dynamics evolves on a finite–dimensional exponentially attracting manifold (3.1). Although we do not rigorously prove such a manifold exists for the present flow, the rapid convergence of model error after the first four flapping cycles suggests that

https://doi.org/10.1017/jfm.2026.11742 Published online by Cambridge University Press

the system quickly enters this slaved regime, enabling (3.3) to accurately predict the aerodynamic forces and wake structures.

The identified limit cycle represents a dynamic equilibrium between energy generated by the hawkmoth's flapping wings and energy lost due to advection and dissipation. As discussed in § 3.1, kinetic energy is injected into the flow at the fundamental frequency f and is sequentially distributed to higher harmonics via advection-driven ($(\boldsymbol{u}\cdot\nabla)\boldsymbol{u}$) triadic modal interactions. Simultaneously, viscosity ($\nu\nabla^2\boldsymbol{u}$) serves as an energy sink, preferentially dissipating kinetic energy from the flow at smaller scales and higher frequencies. The long-term balance between these energy input, transfer and dissipation effects manifests as the stable limit cycle modelled by (3.3). In this framework, the initial linear term ($n=0$) represents the primary instability caused by wing motion, while subsequent nonlinear terms ($n=1,\ 2,\ 3$) encode amplitude-dependent growth and saturation effects, such as advective energy transfer and viscous dissipation. This interpretation is supported by figure 6, which indicates that a single model term ($n=0$) is sufficient to perturb the system away from equilibrium, while two terms ($n=0,\ 1$; yielding the Stuart–Landau oscillator) are necessary to stabilise the system at the identified limit-cycle amplitude. Furthermore, four terms ($n=0,\ 1,\ 2,\ 3$) are required to model the rapid growth the system undergoes in the early transient period.

In other words, although two terms are sufficient to represent the system's on-attractor dynamics, additional terms are needed to describe the system's behaviour farther away from its limit cycle. We therefore retain four terms in the final model, as the transient accuracy afforded by including higher-order terms is desirable for control applications. A model that underpredicts the system's growth rate (as does the two-term model) would likely lead to inefficient and overconservative control inputs. As mentioned previously, the model (3.3) follows the normal form of a Hopf bifurcation, indicating a limit-cycle dynamics. However, this correspondence should not be taken as evidence a bifurcation has occurred, as such systems are characterised by self-sustaining oscillations that arise when a parameter is varied beyond a critical value. Instead, the present model describes forced oscillations driven by the periodic flapping of the hawkmoth's wings. The effects of this forcing are therefore implicit in the model coefficients μ_n, which determine the speed and trajectory with which the system approaches the identified limit cycle. While the present study focuses solely on hawkmoth hovering, we conjecture that the wake dynamics of other species flying at different speeds may also be represented by normal-form models akin to (3.3), albeit with coefficients μ_n determined by the unique physics of each case.

The rapid initial growth and long-term stability of the wake have significant implications for the hawkmoth's flight performance. It is well established that vortex formation and interaction mechanisms are critical to insects' aerodynamic force production. For example, nearly all insects generate a large wing-attached leading-edge vortex during the downstroke that augments their lift generation (Ellington *et al.* 1996). Additionally, during the stroke reversal period, insect wings interact with the leading-edge vortex generated during the previous half-stroke. These wing–wake interactions can either degrade or enhance lift generation, via mechanisms such as single-vortex suction or breakdown-vortex jets (Chen & Wu 2024; Li & Nabawy 2024). In hawkmoths specifically, prior studies have documented the interactions between multiple vortices that form along their wings (e.g. the leading-edge, trailing-edge and root vortices), as well as the horseshoe-shaped vortex loops shed into their wake (Willmott, Ellington & Thomas 1997; Aono, Shyy & Liu 2009; Warfvinge, Johansson, & Hedenström 2021). However, natural flight conditions are rarely ideal, and many external factors can disrupt the formation of performance-enhancing vortices and wake structures; examples include wind gusts, background turbulence and aerodynamic interference from objects like flowers (Combes &

https://doi.org/10.1017/jfm.2026.11742 Published online by Cambridge University Press

Dudley 2009; Matthews & Sponberg 2018). Because the present model is formulated using a simulation of hovering flight, it cannot predict the exact spatial deformation of a wake impacted by gusts, turbulence or collisions. Despite this, a key implication of the model is that the hawkmoth's wake is robust to such perturbations. For any initial condition within the limit cycle's basin of attraction (i.e. any perturbed state away from quiescence), the dynamics described by (3.3) will naturally guide the system back towards the observed periodic oscillations. This intrinsic stability ensures a rapid recovery of force-enhancing wake structures following a transient disturbance. Therefore, the model indicates that the hawkmoth not only possesses an effective mechanism for generating lift and thrust, but one that is inherently robust, a vital attribute for navigating complex natural environments.

In this work, we employ fixed periodic wing kinematics to investigate the dynamics of only the hovering hawkmoth's wake, absent any changes in body attitude or wing kinematics. Our findings regarding wake stability therefore complement prior analyses of the stability of the hawkmoth's flight system (Gao, Aono & Liu 2009; Kim & Han 2014). For example, Cheng, Deng & Hedrick (2011) consider the dynamics of a pitching manoeuvre, concluding that hawkmoths employ active feedback to adjust their orientation. Furthermore, they demonstrate this control mechanism is stable (i.e. the body pitching angle remains less than 90°), even when incorporating sensory latency of more than two flapping periods. In addition to sensory delays, the settling time we compute for the wake dynamics ($t_s/T = 4.42$) likely also influences the hawkmoth's manoeuvrability. For example, if wake stabilisation is slow compared with adjustments in body attitude and wing motion, the flow would effectively retain an aerodynamic 'memory' of prior states, adding latency to the time it takes for the hawkmoth to respond to disturbances. Exploration of the relationship between the hawkmoth's wake dynamics and that of its flight control system represents a promising avenue for future research.

3.4. *Limitations and future directions*

The reduced-order dynamic model (3.3) achieves our stated goal of capturing the wake's transition from quiescence to periodicity. Moreover, it accurately reflects the long-term stability of the hawkmoth's wake dynamics and associated force generation. However, it underpredicts aerodynamic forces, particularly lift, during the first few flapping cycles ($t/T \approx 0.0$–4.0, figure 8). Two principal aspects of our modelling strategy contribute to this early transient error. First, the discrepancy partly stems from using spatial modes derived from the limit cycle to model the transient dynamics. This choice, as noted in section § 3.1, is rooted in the understanding that a periodic vortex shedding dynamics typically approaches a stable attractor (Wiliamson 1996; Noack *et al.* 2003). Consequently, modes characterising this attractor capture the most persistent and energetically dominant flow features, providing an ideal basis for a parsimonious low-order dynamic model. The trade-off is that this modal basis may not completely span early short-lived flow structures that exist before convergence to the identified limit cycle. Wake capture, for example, occurs when the wings interact with the wake shed during previous strokes (Birch & Dickinson 2003); consequently, its effects are diminished during the first half-stroke while the wake is still developing. Such a transient dynamics significantly influences force generation during the initial flapping cycles, as wing–wake interactions can either enhance or reduce lift depending on wing–wake phasing (Lua, Lim & Yeo 2011). This is evident in the observation that the CFD forces become periodic only after five flapping cycles (figure 11(*b*), Appendix B).

Second, modelling error also arises from enforcing a low-dimensional manifold structure, identified from the periodic response, throughout the entire transient history

https://doi.org/10.1017/jfm.2026.11742 Published online by Cambridge University Press

of the wake. As detailed in section § 3.1, (3.1) maps higher-frequency DMD modes as nonlinear functions of the fundamental pair $\alpha_{1,2}$. This approach is consistent with the slaving principle and inertial manifold theory, which suggests that the long-term dynamics in dissipative systems is governed by a few slow driving variables, to which other variables are enslaved (Haken 1977; Sirovich *et al.* 1990; Temam 2012). By enforcing these relationships throughout the transient, we aim for the simplest model describing the system's transition from quiescence to its stable limit cycle. As before, this simplification prioritises interpretability by focusing on the persistent low-dimensional dynamics; however, it comes at the cost of some accuracy during the early transient when these slaving relationships are not yet fully established. Together, these limitations suggest that the model does not capture the exact energy pathways and vortex interaction mechanisms active throughout the hawkmoth's first few flapping cycles. Prior studies have addressed similar shortcomings by performing a separate decomposition of the transient flow data, then using interpolation to continuously deform the transient spatial modes towards the limit-cycle-derived modes (Stankiewicz *et al.* 2017; Loiseau *et al.* 2018). Alternatively, autoencoder neural networks or other manifold learning techniques may be employed to more precisely identify the nonlinear interactions characterising the startup dynamics (Tenenbaum *et al.* 2000; Champion *et al.* 2019; Fresca & Manzoni 2022). However, such approaches would necessarily complicate the model, leading to increased dimensionality and potential loss of interpretability.

Despite limitations in capturing early transient behaviour (due largely to deliberate modelling choices), the present ROM (3.3) successfully resolves the system's near/on-limit-cycle dynamics, enabling accurate estimation of the hawkmoth's long-term wake generation and force production. As such, it offers a simple foundation for future investigations of biological propulsion systems. Although we focus solely on an individual hovering hawkmoth's wake, our order-reduction methodology and overall conclusions are more broadly applicable. Analogous models may be derived for other insects and flight modes, enabling cross-species comparison of wake stability and energy transfer mechanisms. We note, however, that extension of this methodology to forward flight is somewhat complicated by a non-zero base flow past the insect's body; such cases motivate incorporating a shift mode ($\boldsymbol{\Phi}_{\Delta} = \boldsymbol{\Phi}_{mean} - \boldsymbol{U}_{base}$), as proposed in studies of bluff body wakes (Noack *et al.* 2003; Stankiewicz *et al.* 2017). Furthermore, insects are not the only animals that locomote via periodically forced vortex shedding. Other biological examples include undulatory fish swimming (Menzer *et al.* 2022; Guo *et al.* 2023) and metachronal rowing in ctenophores and crustaceans (Lionetti *et al.* 2023; Herrera-Amaya *et al.* 2025). Similar principles regarding wake stability and limit-cycle dynamics likely extend to these species as well, although this remains to be confirmed by future studies.

The collapse of the hawkmoth's complex wake dynamics onto a stable 2-D attractor has strong implications for the design and control of bio-inspired flapping-wing flight systems. Such a low-dimensional representation is amenable to control strategies, with model coefficients μ_n potentially parameterised by Reynolds number or wing kinematics. However, parameterisation would require expanding the modal basis to span the relevant parameter space (Brunton, Proctor, & Kutz 2016*b*; Conti *et al.* 2023). While the efficacy of such an extension is a subject for future study, the present results confirm that the underlying wake dynamics is suitably low-dimensional to make flow prediction and control strategies feasible. Additionally, while we employ fixed periodic wing kinematics, real insects modulate their wing motion and body posture in response to environmental stimuli. Previous works have shown that, through various mechanisms, such kinematic modifications help stabilise the insect's body orientation following a perturbation (Ristroph *et al.* 2010; Taha *et al.* 2020; Hedrick *et al.* 2024). Exploration

https://doi.org/10.1017/jfm.2026.11742 Published online by Cambridge University Press

of the dynamic coupling between the hawkmoth's stable wake dynamics and adaptive body/wing kinematics is a promising avenue for developing robust, agile and controllable micro-aerial vehicles (MAVs).

Furthermore, the wake stability modelled in the present study is just one aspect of a more complex feedback loop that dictates the hawkmoth's ability to manoeuvre effectively. For example, following a gust of wind, the hawkmoth's wing kinematics and body posture will be passively impacted by changes in aerodynamic loading. Such changes will then be detected by the insect's sensory feedback system (e.g. the campaniform sensilla distributed along its wings), resulting in an active control response to the perturbation. The time it takes for the wake to reflect these active changes in wing kinematics further dictates how quickly the insect can recover. Our future efforts will focus on expanding the current modelling framework to incorporate different aspects of this wider control loop (e.g. sensory feedback, body stabilisation, variable wing kinematics, etc.).

4. Conclusion

In this work, we identified what is, to our knowledge, the first reduced-order model for a hovering hawkmoth's wake dynamics. We began by performing DMD on CFD simulation data of hovering hawkmoth flight. Then, we identified nonlinear harmonic relationships among the DMD modes, reducing system dimensionality to just the leading mode pair. Finally, we employed SINDy to uncover a parsimonious and interpretable dynamic model governing the wake's evolution. The resulting model is a Stuart–Landau oscillator with higher-order nonlinear terms, indicating that the wake dynamics is characterised by stable limit-cycle oscillations. We propose that this inherent stability stems from a dynamic equilibrium between energy injected by the flapping wings, advective energy transfer across scales and viscous dissipation. This interpretive framework for analysing wake dynamics complements prior studies of flight stability in hawkmoths, which have largely focused on stability of body orientation and wing kinematics. In nature, insects frequently encounter wind gusts and other aerodynamic perturbations. Following such perturbations, the limit-cycle attractor provides a mechanism for rapid recovery of wake structures critical to the hawkmoth's aerodynamic performance (e.g. the leading-edge vortex). Finally, we note that, although the model is less accurate during the initial startup, it successfully captures the hawkmoth's long-term periodic wake dynamics. This work demonstrates that even complex biological flows can be approximated by a simple low-order dynamics, offering inspiration for the design and control of bio-inspired MAVs.

Acknowledgements. All simulations and algorithms were run on the high-performance computing cluster at Case Western Reserve University.

Funding. This work is supported by the National Science Foundation (NSF CBET-2453175) and the Air Force Office of Scientific Research (AFOSR FA9550-24-1-0122).

Declaration of interests. The authors report no conflict of interest.

Appendix A. Simulation set-up and grid independence

Figure 10(*a*) shows the computational domain employed in the simulation (§ 2.1). The domain mesh has dimensions $225 \times 257 \times 193 \approx 11$ M and is divided into three layers. A dense layer contains the flapping wing, a secondary dense layer surrounds all wake structures and a stretched layer extends to the domain boundaries. The stretched layer serves only to mitigate boundary effects; we therefore apply DMD and the wake survey method to the subdomain consisting of the two dense layers. All domain boundaries are assigned a zero gradient boundary condition. Figure 10(*b*) provides a close-up of

https://doi.org/10.1017/jfm.2026.11742 Published online by Cambridge University Press

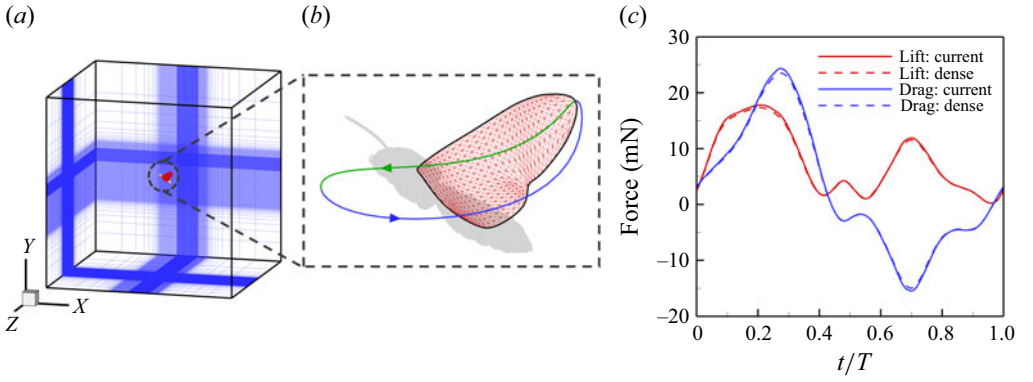


Figure 10. (*a*) Computational domain (blue) containing ∼17 M elements, with the simulated flapping wing (red) situated at the centre of the domain. (*b*) Close-up of the meshed wing. Its downstroke and upstroke wing-tip trajectories are shown in green and blue, respectively. (*c*) Grid convergence comparison between current (∼11 M) and dense (∼17 M) meshes. The hawkmoth's aerodynamic lift (red) and drag (blue) are shown throughout the sixth flapping cycle.

the hawkmoth wing mesh, with its downstroke wing-tip trajectory shown in green and upstroke trajectory shown in blue.

To test for grid independence, we rerun the simulation using a denser computational grid ($257 \times 289 \times 225 \approx 17$ M), containing ∼1.5 times the elements in the original mesh. Figure 10(*c*) compares these two grids, showing the instantaneous forces produced by the wing during the sixth flapping cycle. We calculate differences of 2.3 % and 3.7 % in cycle-averaged lift and drag, respectively, indicating convergence. Therefore, to minimise computational cost, we employ the smaller grid (≈ 11 M) throughout this study.

Appendix B. Evaluation of periodicity

Our modelling strategy requires extracting modes from the wake once it has reached a periodic state. To measure periodicity, we introduce the criterion $\delta_{\boldsymbol{U}} = ||\boldsymbol{U}(t) - \boldsymbol{U}(t + T)||_F / D$, equivalent to

$$\delta_{\boldsymbol{U}} = \sqrt{\sum_{i=1}^{D} \left((u_i\,(t) - u_i(t+T))^2 + (v_i\,(t) - v_i(t+T))^2 + (w_i\,(t) - w_i(t+T))^2\right)/D}, \tag{A1}$$

where $D \approx 7$ M is the size of the subdomain used for DMD; $T = 39$ ms is the hawkmoth's flapping period; and u, v and w are velocity components in the x, y and z directions, respectively. As shown in figure 11(*a*), $\delta_{\boldsymbol{U}}$ reaches a small and steady value around $t/T \approx 9.0$; we conclude that the wake becomes periodic after nine flapping cycles.

We also evaluate how long it takes for the hawkmoth's force production to become periodic. Figure 11(*b*) plots the difference in force output between neighbouring flapping cycles (i.e. $F(t) - F(t + T)$). Results are shown for drag, lift, lateral and total forces. For all values, the difference drops to nearly zero around $t/T \approx 5.0$, indicating that the hawkmoth's force generation becomes periodic after five flapping cycles. Notably, the wake requires nearly twice as long to achieve periodicity (nine flapping cycles) as the forces (five flapping cycles); this suggests that the hawkmoth's force production is unaffected by small aperiodicities in the surrounding flow. As explained in § 3.1, we perform DMD on the fifteenth flapping cycle, by which point both the wake and forces are periodic.

https://doi.org/10.1017/jfm.2026.11742 Published online by Cambridge University Press

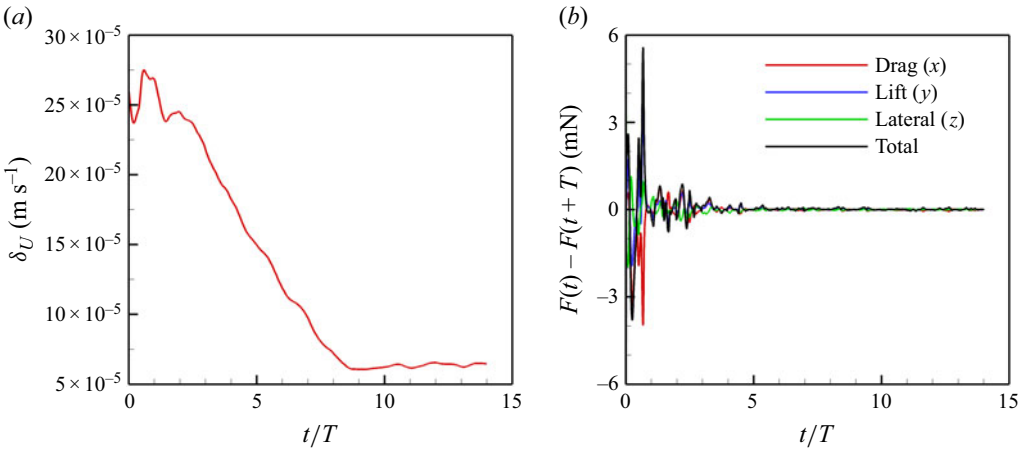


Figure 11. (*a*) Periodicity of the hawkmoth's wake, evaluated using δ_U (A1). (*b*) Periodicity of the hawkmoth's force generation, evaluated using the difference between neighbouring flapping cycles ($F(t) - F(t+T)$). Results are shown for the drag (red), lift (blue), lateral (green) and total (black) forces. In both panels, data are not included for the final simulated flapping cycle ($t/T = 14.0$–15.0), as there is no subsequent cycle for comparison.

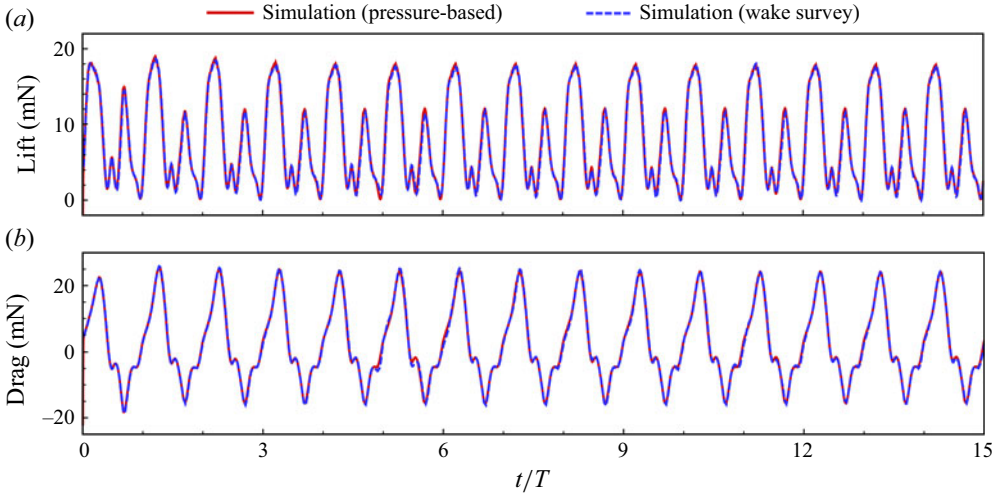


Figure 12. Comparison of aerodynamic (*a*) lift and (*b*) drag forces from our CFD simulation (red) and the wake survey method (blue).

Appendix C. Validation of wake survey method

Here, we evaluate whether the wake survey method (§ 2.4) accurately reproduces the aerodynamic lift and drag generated by the hawkmoth. Figure 12 compares the forces computed using pressure data from our CFD solver with results from the velocity-only wake survey method. The wake survey results closely match those from the simulation, with a mean absolute error of 0.40 mN (2.8 % of the hawkmoth's body weight). We therefore conclude that this method is suitable for assessing the accuracy of our ROM.

https://doi.org/10.1017/jfm.2026.11742 Published online by Cambridge University Press

β_0	1.450×10^{-3}	$\beta_{33,34}$	$(-3.310\mp11.78i)\times10^{-53}$	$\beta_{65,66}$	$(1.323\pm14.33i)\times10^{-103}$
$\beta_{3,4}$	$(-38.92\pm2.236i)\times10^{-5}$	$\beta_{35,36}$	$(5.920\pm5.155i)\times10^{-56}$	$\beta_{67,68}$	$(-9.096\mp3.115i)\times10^{-107}$
$\beta_{5,6}$	$(-1.182\pm1.248i)\times10^{-7}$	$\beta_{37,38}$	$(-49.93\pm8.573i)\times10^{-60}$	$\beta_{69,70}$	$(-64.28\mp2.059i)\times10^{-111}$
$\beta_{7,8}$	$(-1.286\mp8.413i)\times10^{-11}$	$\beta_{39,40}$	$(-2.429\pm2.212i)\times10^{-62}$	$\beta_{71,72}$	$(4.153\mp1.164i)\times10^{-113}$
$\beta_{9,10}$	$(-1.496\pm4.340i)\times10^{-14}$	$\beta_{41,42}$	$(-7.147\pm20.14i)\times10^{-65}$	$\beta_{73,74}$	$(2.477\mp1.497i)\times10^{-116}$
$\beta_{11,12}$	$(2.271\pm1.286i)\times10^{-17}$	$\beta_{43,44}$	$(-13.79\mp2.116i)\times10^{-69}$	$\beta_{75,76}$	$(-8.623\mp17.45i)\times10^{-120}$
$\beta_{13,14}$	$(-15.13\pm1.208i)\times10^{-21}$	$\beta_{45,46}$	$(-8.542\pm3.230i)\times10^{-72}$	$\beta_{77,78}$	$(-7.389\mp10.85i)\times10^{-123}$
$\beta_{15,16}$	$(2.669\mp8.495i)\times10^{-24}$	$\beta_{47,48}$	$(-3.915\mp4.531i)\times10^{-75}$	$\beta_{79,80}$	$(-88.73\pm1.085i)\times10^{-127}$
$\beta_{17,18}$	$(-2.977\pm4.407i)\times10^{-27}$	$\beta_{49,50}$	$(-1.121\pm3.771i)\times10^{-78}$	$\beta_{81,82}$	$(5.923\mp1.096i)\times10^{-129}$
$\beta_{19,20}$	$(6.251\pm322.9i)\times10^{-32}$	$\beta_{51,52}$	$(2.131\pm1.468i)\times10^{-81}$	$\beta_{83,84}$	$(1.193\mp3.921i)\times10^{-132}$
$\beta_{21,22}$	$(19.57\pm1.864i)\times10^{-34}$	$\beta_{53,54}$	$(-8.608\pm14.16i)\times10^{-85}$	$\beta_{85,86}$	$(-27.30\pm6.058i)\times10^{-136}$
$\beta_{23,24}$	$(-11.50\mp4.270i)\times10^{-37}$	$\beta_{55,56}$	$(-8.646\pm112.0i)\times10^{-89}$	$\beta_{87,88}$	$(19.09\pm1.658i)\times10^{-139}$
$\beta_{25,26}$	$(5.784\mp4.961i)\times10^{-40}$	$\beta_{57,58}$	$(2.885\pm6.837i)\times10^{-91}$	$\beta_{89,90}$	$(2.257\mp12.97i)\times10^{-142}$
$\beta_{27,28}$	$(7.404\mp47.131i)\times10^{-44}$	$\beta_{59,60}$	$(3.619\pm3.312i)\times10^{-94}$	$\beta_{91,92}$	$(-8.283\pm3.724i)\times10^{-145}$
$\beta_{29,30}$	$(2.518\mp1.656i)\times10^{-46}$	$\beta_{61,62}$	$(30.96\pm9.909i)\times10^{-98}$	$\beta_{93,94}$	$(-4.824\mp4.039i)\times10^{-148}$
$\beta_{31,32}$	$(5.085\mp18.45i)\times10^{-50}$	$\beta_{63,64}$	$(-21.55\pm1.549i)\times10^{-101}$		

Table 2. Coefficients β_i corresponding to the low-dimensional manifold defined by (3.1).

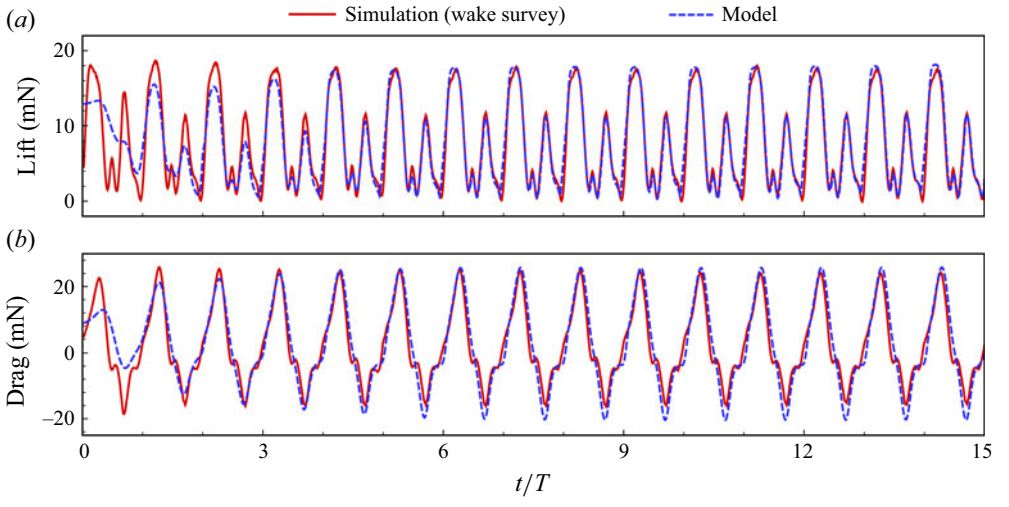


Figure 13. Comparison of aerodynamic (*a*) lift and (*b*) drag forces from our CFD simulation (red) and the reduced-order model (blue). All forces are computed using the velocity-based wake survey method.

Appendix D. Manifold constants

Table 2 provides the constants corresponding to the low-dimensional manifold defined by (3.1).

Appendix E. Modelling error

The discrepancy in forces visible in figure 8 represents a combination of errors introduced by the modelling process and the force estimation technique (i.e. the wake survey method). Figure 13 helps decouple these sources of error. This figure is identical to figure 8, except the CFD forces (red lines) are computed using the wake survey method, ensuring that the

https://doi.org/10.1017/jfm.2026.11742 Published online by Cambridge University Press

same force calculation technique is applied to both the CFD and ROM (3.3). From the lift data, we compute a post-transient ($t/T = 5.0$–15.0) mean absolute error of 0.52 mN, which represents the intrinsic error of the modelling process.

References

Aono, H., Shyy, W. & Liu, H. 2009 Near wake vortex dynamics of a hovering hawkmoth. *Acta Mechanica Sin.* **25**, 23–36.

Billings, S.A. 2013 *Nonlinear System Identification: NARMAX Methods in the Time, Frequency, and Spatio-Temporal Domains*. John Wiley & Sons.

Birch, J.M. & Dickinson, M.H. 2003 The influence of wing–wake interactions on the production of aerodynamic forces in flapping flight. *J. Expl Biol.* **206** (13), 2257–2272.

Brunton, S.L., Proctor, J.L. & Kutz, J.N. 2016*a* Discovering governing equations from data by sparse identification of nonlinear dynamical systems. *Proc. Natl Acad. Sci.* **113** (15), 3932–3937.

Brunton, S.L., Proctor, J.L. & Kutz, J.N. 2016*b* Sparse identification of nonlinear dynamics with control (SINDYc). *IFAC-PapersOnLine* **49** (18), 710–715.

Brunton, S.L., Rowley, C.W. & Williams, D.R. 2013 Reduced-order unsteady aerodynamic models at low Reynolds numbers. *J. Fluid Mech.* **724**, 203–233.

Callaham, J.L., Brunton, S.L. & Loiseau, J.-C. 2022 On the role of nonlinear correlations in reduced-order modelling. *J. Fluid Mech.* **938**, A1.

Champion, K., Lusch, B., Kutz, J.N. & Brunton, S.L. 2019 Data-driven discovery of coordinates and governing equations. *Proc. Natl Acad. Sci.* **116** (45), 22445–22451.

Chen, L. & Wu, J. 2024 Coexistence of dual wing–wake interaction mechanisms during the rapid rotation of flapping wings. *J. Fluid Mech.* **987**, A16.

Cheng, B., Deng, X. & Hedrick, T.L. 2011 The mechanics and control of pitching manoeuvres in a freely flying hawkmoth (Manduca sexta). *J. Expl Biol.* **214** (24), 4092–4106.

Combes, S.A. & Dudley, R. 2009 Turbulence-driven instabilities limit insect flight performance. *Proc. Natl Acad. Sci.* **106** (22), 9105–9108.

Conti, P., Gobat, G., Fresca, S., Manzoni, A. & Frangi, A. 2023 Reduced order modeling of parametrized systems through autoencoders and SINDy approach: continuation of periodic solutions. *Comput. Meth. Appl. Mech. Engng* **411**, 116072.

Dickinson, M.H., Lehmann, F.-O. & Sane, S.P. 1999 Wing rotation and the aerodynamic basis of insect flight. *Science* **284** (5422), 1954–1960.

Ellington, C.P. 1984 The aerodynamics of hovering insect flight. I. The quasi-steady analysis. *Phil. Trans. R. Soc. Lond. B Biol. Sci.* **305** (1122), 1–15.

Ellington, C.P., Van Den Berg, C., Willmott, A.P. & Thomas, A.L. 1996 Leading-edge vortices in insect flight. *Nature* **384** (6610), 626–630.

Fresca, S. & Manzoni, A. 2022 POD-DL-ROM: enhancing deep learning-based reduced order models for nonlinear parametrized PDEs by proper orthogonal decomposition. *Comput. Meth. Appl. Mech. Engng* **388**, 114181.

Gao, N., Aono, H. & Liu, H. 2009 A numerical analysis of dynamic flight stability of hawkmoth hovering. *J. Biomech. Sci. Engng* **4** (1), 105–116.

Guo, J., Han, P., Zhang, W., Wang, J., Lauder, G.V., Di Santo, V. & Dong, H. 2023 Vortex dynamics and fin-fin interactions resulting in performance enhancement in fish-like propulsion. *Phys. Rev. Fluids* **8** (7), 073101.

Haider, N., Lou, Z., Hsu, S.-J., Cheng, B. & Li, C. 2025 Flapping dynamics and wing flexibility enhance odor detection in blue bottle flies. *Bioinspir. Biomim.* **20** (2), 026025.

Haken, H. 1977 Synergetics. *Phys. Bull.* **28** (9), 412.

Hedrick, T.L., Blandford, E. & Taha, H.E. 2024 Biomechanics of insect flight stability and perturbation response. *Integrat. Comput. Biol.* **64** (2), 611–618.

Herbert, T. 1988 Secondary instability of boundary layers. *Annu. Rev. Fluid Mech.* **20**, 487–526.

Herrera-Amaya, A., Tack, N.B., Lou, Z., Li, C. & Wilhelmus, M.M. 2025 The effects of temperature and viscosity on the metachronal swimming of crustaceans. arXiv preprint arXiv: 2504.04236.

Holmes, P. 2012 *Turbulence, Coherent Structures, Dynamical Systems and Symmetry*. Cambridge University Press.

Kaptanoglu, A.A., Morgan, K.D., Hansen, C.J. & Brunton, S.L. 2021 Physics-constrained, low-dimensional models for magnetohydrodynamics: first-principles and data-driven approaches. *Phys. Rev. E* **104** (1), 015206.

https://doi.org/10.1017/jfm.2026.11742 Published online by Cambridge University Press

KIM, J.-K. & HAN, J.-H. 2014 A multibody approach for 6-DOF flight dynamics and stability analysis of the hawkmoth Manduca sexta. *Bioinspir. Biomim.* **9** (1), 016011.
KINJANGI, D.K. & FOTI, D. 2023 Characterization of energy transfer and triadic interactions of coherent structures in turbulent wakes. *J. Fluid Mech.* **971**, A7.
LEHMANN, F.-O. 2004 The mechanisms of lift enhancement in insect flight. *Naturwissenschaften* **91**, 101–122.
LI, H. & NABAWY, M.R. 2024 Detachment of leading-edge vortex enhances wake capture force production. *J. Fluid Mech.* **995**, A6.
LI, C., WANG, J. & DONG, H. 2017 Proper orthogonal decomposition analysis of flapping hovering wings. In *Paper presented at the 55th AIAA Aerospace Sciences Meeting*.
LIANG, Z. & DONG, H. 2015 On the symmetry of proper orthogonal decomposition modes of a low-aspect-ratio plate. *Phys. Fluids* **27** (6), 063601.
LIANG, B. & SUN, M. 2013 Nonlinear flight dynamics and stability of hovering model insects. *J. R. Soc. Interface* **10** (85), 20130269.
LIONETTI, S., HEDRICK, T.L. & LI, C. 2022 Aerodynamic explanation of flight speed limits in hawkmoth-like flapping-wing insects. *Phys. Rev. Fluids* **7** (9), 093104.
LIONETTI, S., LOU, Z., HERRERA-AMAYA, A., BYRON, M.L. & LI, C. 2023 A new propulsion enhancement mechanism in metachronal rowing at intermediate Reynolds numbers. *J. Fluid Mech.* **974**, A45.
LOISEAU, J.-C., BRUNTON, S.L. & NOACK, B.R. 2018 From the POD-Galerkin method to sparse manifold models. In *Handbook on Model Order Reduction*. De Gruyter GmbH.
LOU, Z., LEI, M., DONG, H. & LI, C. 2024 Wing–antenna interaction reduces odour fatigue in butterfly odour-tracking flight. *J. Fluid Mech.* **998**, A45.
LUA, K.B., LIM, T. & YEO, K. 2011 Effect of wing–wake interaction on aerodynamic force generation on a 2D flapping wing. *Exp. Fluids* **51** (1), 177–195.
LUMLEY, J.L. 1967 The structure of inhomogeneous turbulent flows. In *Atmospheric Turbulence and Radio Wave Propagation* (ed. A.M. Yaglom & V.I. Tartarsky), pp. 166–178. Publishing House Nauka.
MATTHEWS, M. & SPONBERG, S. 2018 Hawkmoth flight in the unsteady wakes of flowers. *J. Expl Biol.* **221** (22), jeb179259.
MENON, K. & MITTAL, R. 2021*a* On the initiation and sustenance of flow-induced vibration of cylinders: insights from force partitioning. *J. Fluid Mech.* **907**, A37.
MENON, K. & MITTAL, R. 2021*b* Quantitative analysis of the kinematics and induced aerodynamic loading of individual vortices in vortex-dominated flows: a computation and data-driven approach. *J. Comput. Phys.* **443**, 110515.
MENZER, A., GONG, Y., FISH, F.E. & DONG, H. 2022 Bio-inspired propulsion: towards understanding the role of pectoral fin kinematics in manta-like swimming. *Biomimetics* **7** (2), 45.
MITTAL, R., DONG, H., BOZKURTTAS, M., NAJJAR, F., VARGAS, A. & VON LOEBBECKE, A. 2008 A versatile sharp interface immersed boundary method for incompressible flows with complex boundaries. *J. Comput. Phys.* **227** (10), 4825–4852.
NOACK, B.R., AFANASIEV, K., MORZYŃSKI, M., TADMOR, G. & THIELE, F. 2003 A hierarchy of low-dimensional models for the transient and post-transient cylinder wake. *J. Fluid Mech.* **497**, 335–363.
NOCA, F., SHIELS, D. & JEON, D. 1997 Measuring instantaneous fluid dynamic forces on bodies, using only velocity fields and their derivatives. *J. Fluids Struct.* **11** (3), 345–350.
RISTROPH, L., BERGOU, A.J., RISTROPH, G., COUMES, K., BERMAN, G.J., GUCKENHEIMER, J. & COHEN, I. 2010 Discovering the flight autostabilizer of fruit flies by inducing aerial stumbles. *Proc. Natl Acad. Sci.* **107** (11), 4820–4824.
SANE, S.P. 2003 The aerodynamics of insect flight. *J. Expl Biol.* **206** (23), 4191–4208.
SCHLEGEL, M. & NOACK, B.R. 2015 On long-term boundedness of Galerkin models. *J. Fluid Mech.* **765**, 325–352.
SCHMID, P.J. 2010 Dynamic mode decomposition of numerical and experimental data. *J. Fluid Mech.* **656**, 5–28.
SCHMIDT, O.T. 2020 Bispectral mode decomposition of nonlinear flows. *Nonlinear Dyn.* **102** (4), 2479–2501.
SIEBER, M., PASCHEREIT, C.O. & OBERLEITHNER, K. 2016 Spectral proper orthogonal decomposition. *J. Fluid Mech.* **792**, 798–828.
DE SILVA, B., CHAMPION, K., QUADE, M., LOISEAU, J.-C., KUTZ, J.N. & BRUNTON, S. 2020 PySINDy: a python package for the sparse identification of nonlinear dynamical systems from data. *J. Open Source Softw.* **5** (49), 1–4.
SIROVICH, L., KNIGHT, B. & RODRIGUEZ, J. 1990 Optimal low-dimensional dynamical approximations. *Q. Appl. Math.* **48** (3), 535–548.

https://doi.org/10.1017/jfm.2026.11742 Published online by Cambridge University Press

STANKIEWICZ, W., MORZYŃSKI, M., KOTECKI, K. & NOACK, B.R. 2017 On the need of mode interpolation for data-driven Galerkin models of a transient flow around a sphere. *Theor. Comput. Fluid Dyn.* **31**, 111–126.

TAHA, H.E., KIANI, M., HEDRICK, T.L. & GREETER, J.S. 2020 Vibrational control: a hidden stabilization mechanism in insect flight. *Sci. Robot.* **5** (46), eabb1502.

TAIRA, K., BRUNTON, S.L., DAWSON, S.T., ROWLEY, C.W., COLONIUS, T., MCKEON, B.J. & UKEILEY, L.S. 2017 Modal analysis of fluid flows: an overview. *AIAA J.* **55** (12), 4013–4041.

TEMAM, R. 2012 *Infinite-Dimensional Dynamical Systems in Mechanics and Physics*, vol. 68. Springer Science & Business Media.

TENENBAUM, J.B., SILVA, V.D & LANGFORD, J.C. 2000 A global geometric framework for nonlinear dimensionality reduction. *Science* **290** (5500), 2319–2323.

TU, J.H. 2013 *Dynamic Mode Decomposition: Theory and Applications*. Princeton University.

WANG, Z.J. 2005 Dissecting insect flight. *Annu. Rev. Fluid Mech.* **37** (1), 183–210.

WANG, Z., ZHANG, G., ZHOU, B., SUN, T. & WU, J. 2024 Identification of control equations using low-dimensional flow representations of pitching airfoil. *Phys. Fluids* **36** (4), 045128.

WARFVINGE, K., JOHANSSON, L.C. & HEDENSTRÖM, A. 2021 Hovering flight in hummingbird hawkmoths: kinematics, wake dynamics and aerodynamic power. *J. Expl Biol.* **224** (10), jeb230920.

WEIS-FOGH, T. 1973 Quick estimates of flight fitness in hovering animals, including novel mechanisms for lift production. *J. Expl Biol.* **59** (1), 169–230.

WILIAMSON, C. 1996 Vortex dynamics in the cylinder wake. *Annu. Rev. Fluid Mech.* **28**, 477–539.

WILLMOTT, A.P., ELLINGTON, C.P. & THOMAS, A.L. 1997 Flow visualization and unsteady aerodynamics in the flight of the hawkmoth, Manduca sexta. *Phil. Trans. R. Soc. Lond. Ser. B: Biol. Sci.* **352** (1351), 303–316.

https://doi.org/10.1017/jfm.2026.11742 Published online by Cambridge University Press